

Spontaneous mirror-symmetry breaking induces inverse energy cascade in 3D active fluids

Jonasz Słomka^a and Jörn Dunkel^{a,1}

^aDepartment of Mathematics, Massachusetts Institute of Technology, Cambridge, MA 02139-4307

Edited by David A. Weitz, Harvard University, Cambridge, MA, and approved January 4, 2017 (received for review September 2, 2016)

Classical turbulence theory assumes that energy transport in a 3D turbulent flow proceeds through a Richardson cascade whereby larger vortices successively decay into smaller ones. By contrast, an additional inverse cascade characterized by vortex growth exists in 2D fluids and gases, with profound implications for meteorological flows and fluid mixing. The possibility of a helicity-driven inverse cascade in 3D fluids had been rejected in the 1970s based on equilibrium-thermodynamic arguments. Recently, however, it was proposed that certain symmetry-breaking processes could potentially trigger a 3D inverse cascade, but no physical system exhibiting this phenomenon has been identified to date. Here, we present analytical and numerical evidence for the existence of an inverse energy cascade in an experimentally validated 3D active fluid model, describing microbial suspension flows that spontaneously break mirror symmetry. We show analytically that self-organized scale selection, a generic feature of many biological and engineered nonequilibrium fluids, can generate parity-violating Beltrami flows. Our simulations further demonstrate how active scale selection controls mirror-symmetry breaking and the emergence of a 3D inverse cascade.

active turbulence | inverse cascade | Beltrami flows | pattern formation

Turbulence, the chaotic motion of liquids and gases, remains one of the most widely studied phenomena in classical physics (1, 2). Turbulent flows determine energy transfer and material mixing over a vast range of scales, from the interstellar medium (3, 4) and solar winds (5) to the Earth's atmosphere (6, 7), ocean currents (8), and our morning cup of coffee. Of particular recent interest is the interplay of turbulence and active biological matter (9), owing to its relevance for carbon fixation and nutrient transport in marine ecosystems (10). Although much has been learned about the statistical and spectral properties of turbulent flows both experimentally (11–13) and theoretically (14–21) over the last 75 years, several fundamental physical and mathematical (22) questions still await their answer. One of the most important among them, with profound implications for the limits of hydrodynamic mixing, concerns whether 3D turbulent flows can develop an inverse cascade that transports energy from smaller to larger scales (19, 23, 24).

Kolmogorov's 1941 theory of turbulence (14) assumes that turbulent energy transport in 3D proceeds primarily from larger to smaller scales through the decay of vortices. This forward (Richardson) cascade is a consequence of the fact that the 3D inviscid Euler equations conserve energy (1). In 1967, Kraichnan (17) realized that the presence of a second conserved quantity, enstrophy, in 2D turbulent flows implies the existence of two dual cascades (25): a vorticity-induced cascade to smaller scales and an inverse energy cascade to larger scales (20, 26). Two years later, Moffatt (27) discovered a new invariant of the 3D Euler equations, which he termed helicity. Could helicity conservation generate an inverse turbulent cascade in 3D? Building on thermodynamic considerations, Kraichnan (23) argued in 1973 that this should not be possible, but he also conceded that turbulent flows do not necessarily follow equilibrium statistics. Since then, insightful theoretical studies (19, 24) have elucidated other important conditions for the emergence of helicity-driven inverse

cascades in 3D fluids, in particular identifying mirror-symmetry breaking as a key mechanism (24). However, no natural or artificially engineered fluid system exhibiting this phenomenon has been identified to date.

Here, we predict that fluid flows in active nonequilibrium liquids, such as bacterial suspensions, can spontaneously break mirror symmetry, resulting in a 3D inverse cascade. Broken mirror symmetry plays an important role in nature, exemplified by the parity-violating weak interactions (28) in the standard model of particle physics, by the helical structure of DNA (29) or, at the macroscale, by chiral seed pods (30). Another, fluid-based realization (31) of a spontaneously broken chiral symmetry was recently observed in confined bacterial suspensions (32, 33), which form stable vortices of well-defined circulation when the container dimensions match the correlation scale $\sim 70 \mu\text{m}$ of the collective cell motion in bulk (34, 35). Motivated by these observations, we investigate a generalized Navier–Stokes model (36, 37) for pattern-forming nonequilibrium fluids that are driven by an active component, which could be swimming bacteria (34, 35) or ATP-driven microtubules (38, 39) or artificial microswimmers (40–42). The theory uses only generic assumptions about the symmetries and long-wavelength structure of active stress tensors and captures the experimentally observed bulk vortex dynamics in 3D bacterial suspensions (34, 35) and in flows driven by isotropic active microtubule networks (38) (Fig. S1).

To demonstrate the existence of a helicity-driven inverse cascade in 3D active bulk fluids, we first verify analytically the existence of exact parity-violating Beltrami-flow (43–45) solutions. We then confirm numerically that active bulk flows starting from random initial conditions approach attractors that spontaneously break mirror symmetry and are statistically close to Beltrami-vector fields. Finally, we demonstrate that the broken mirror

Significance

Turbulence provides an important mechanism for energy redistribution and mixing in interstellar gases, planetary atmospheres, and the oceans. Classical turbulence theory suggests for ordinary 3D fluids or gases, such as water or air, that larger vortices can transform into smaller ones but not vice versa, thus limiting energy transfer from smaller to larger scales. Our calculations predict that bacterial suspensions and other pattern-forming active fluids can deviate from this paradigm by creating turbulent flow structures that spontaneously break mirror symmetry. These results imply that the collective dynamics of swimming microorganisms can enhance fluid mixing more strongly than previously thought.

Author contributions: J.S. and J.D. designed research; J.S. performed research; and J.S. and J.D. wrote the paper.

The authors declare no conflict of interest.

This article is a PNAS Direct Submission.

Freely available online through the PNAS open access option.

¹To whom correspondence should be addressed. Email: dunkel@math.mit.edu.

This article contains supporting information online at www.pnas.org/lookup/suppl/doi:10.1073/pnas.1614721114/-DCSupplemental.

symmetry leads to an inverse cascade with triad interactions as predicted by Waleffe (19) about 25 years ago.

Results

Theory. We consider pattern-forming nonequilibrium fluids consisting of a passive solvent component, such as water, and a stress-generating active component, which could be bacteria (34), ATP-driven microtubules (38), or Janus particles (46, 47). In contrast to earlier studies, which analyzed the velocity field of the active matter component (35, 48, 49), we focus here on the incompressible solvent velocity field $\mathbf{v}(t, \mathbf{x})$ described by

$$\nabla \cdot \mathbf{v} = 0, \quad \text{[1a]}$$

$$\partial_t \mathbf{v} + \mathbf{v} \cdot \nabla \mathbf{v} = -\nabla p + \nabla \cdot \boldsymbol{\sigma}, \quad \text{[1b]}$$

where $p(t, \mathbf{x})$ is the local pressure. The effective stress tensor $\boldsymbol{\sigma}(t, \mathbf{x})$ comprises passive contributions from the intrinsic solvent fluid viscosity and active contributions representing the stresses exerted by the microswimmers on the fluid (50–53). Experiments (32, 34, 35, 38, 54, 55) show that active stresses typically lead to vortex scale selection in the ambient solvent fluid. This mesoscale pattern formation stands in contrast to the scale-free vortex structures in externally driven classical turbulence and can be described phenomenologically through the stress tensor (36, 37)

$$\boldsymbol{\sigma} = (\Gamma_0 - \Gamma_2 \nabla^2 + \Gamma_4 \nabla^4) [\nabla \mathbf{v} + (\nabla \mathbf{v})^\top], \quad \text{[1c]}$$

where the higher-order derivatives $\nabla^{2n} \equiv (\nabla^2)^n$, $n \geq 2$ account for non-Newtonian effects (56) (*Model Justification*). Such higher-order stresses arise naturally from diagrammatic expansions (57). Similar 1D and 2D models have been studied in the context of soft-mode turbulence and seismic waves (58–60).

The parameters $(\Gamma_0, \Gamma_2, \Gamma_4)$ encode microscopic interactions, thermal and athermal fluctuations, and other nonequilibrium processes. For $\Gamma_2 = \Gamma_4 = 0$, Eq. 1 reduce to the standard Navier–Stokes equations with kinematic viscosity $\Gamma_0 > 0$. For $\Gamma_0 > 0$, $\Gamma_4 > 0$ and $\Gamma_2 < 0$, Eq. 1c defines the simplest ansatz for an active stress tensor that is isotropic, selects flow patterns of a characteristic scale (Fig. 1), and yields a stable theory at small and large wavenumbers (36, 37). The active-to-passive phase transition corresponds to a sign change from $\Gamma_2 < 0$ to $\Gamma_2 > 0$, which can be realized experimentally through ATP or nutrient depletion. The nonnegativity of Γ_0 and Γ_4 follows from stability considerations. Γ_0 describes the damping of long-wavelength perturbations on scales much larger than the correlation length of the coherent flow structures, whereas Γ_2 and Γ_4 account for the growth and damping of modes at intermediate

and small scales (Fig. 1A). The resulting nonequilibrium flow structures can be characterized in terms of the typical vortex size $\Lambda = \pi \sqrt{2\Gamma_4/(-\Gamma_2)}$, growth time scale (37)

$$\tau = \left[\frac{\Gamma_2}{2\Gamma_4} \left(\Gamma_0 - \frac{\Gamma_2^2}{4\Gamma_4} \right) \right]^{-1},$$

circulation speed $U = 2\pi\Lambda/\tau$, and spectral bandwidth (Fig. 1A)

$$\kappa = \left(\frac{-\Gamma_2}{\Gamma_4} - 2\sqrt{\frac{\Gamma_0}{\Gamma_4}} \right)^{1/2}.$$

Specifically, we find $\Lambda = 41 \mu\text{m}$, $U = 57 \mu\text{m/s}$, and $\kappa = 73 \text{mm}^{-1}$ for flows measured in *Bacillus subtilis* suspensions (34, 35) and $\Lambda = 130 \mu\text{m}$, $U = 6.5 \mu\text{m/s}$, and $\kappa = 21 \text{mm}^{-1}$ for ATP-driven microtubule–network suspensions (38) (*Comparison with Experiments*). We emphasize, however, that truncated polynomial stress tensors of the form 1c can provide useful long-wavelength approximations for a broad class of pattern-forming liquids, including magnetically (61), electrically (62), thermally (46, 63, 64), or chemically (47, 65) driven flows.

Exact Beltrami-Flow Solutions and Broken-Mirror Symmetry. The higher-order Navier–Stokes equations defined by Eq. 1 are invariant under the parity transformation $\mathbf{x} \rightarrow -\mathbf{x}$. Their solutions, however, can spontaneously break this mirror symmetry. To demonstrate this explicitly, we construct a family of exact nontrivial stationary solutions in free space by decomposing the Fourier series $\mathbf{v}(t, \mathbf{k})$ of the divergence-free velocity field $\mathbf{v}(t, \mathbf{x})$ into helical modes (19, 24)

$$\mathbf{v}(t, \mathbf{k}) = u^+(t, \mathbf{k}) \mathbf{h}^+(\mathbf{k}) + u^-(t, \mathbf{k}) \mathbf{h}^-(\mathbf{k}), \quad \text{[2]}$$

where \mathbf{h}^\pm are the eigenvectors of the curl operator, $i\mathbf{k} \wedge \mathbf{h}^\pm = \pm k \mathbf{h}^\pm$ with $k = |\mathbf{k}|$. Projecting Eq. 1b onto helicity eigenstates (19) yields the evolution equation for the mode amplitudes u^\pm ,

$$[\partial_t + \xi(k)] u^\pm(t, \mathbf{k}) = \sum_{(\mathbf{p}, \mathbf{q}) : \mathbf{k} = \mathbf{p} + \mathbf{q} = 0} f^\pm(t; \mathbf{k}, \mathbf{p}, \mathbf{q}), \quad \text{[3]}$$

where $\xi(k) = \Gamma_0 k^2 + \Gamma_2 k^4 + \Gamma_4 k^6$ is the active stress contribution, and the nonlinear advection is represented by all triadic interactions (19, 24)

$$f^{sk}(t; \mathbf{k}, \mathbf{p}, \mathbf{q}) = -\frac{1}{4} \sum_{s_p, s_q} (s_p p - s_q q) \left[(\bar{\mathbf{h}}^{s_p} \wedge \bar{\mathbf{h}}^{s_q}) \cdot \bar{\mathbf{h}}^{s_k} \right] \bar{u}^{s_p} \bar{u}^{s_q} \quad \text{[4]}$$

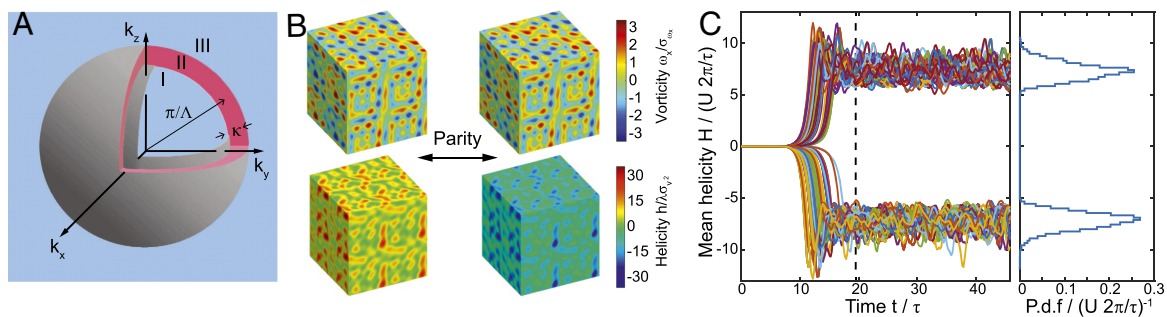


Fig. 1. Exact Beltrami-flow solutions and spontaneous mirror-symmetry breaking in 3D simulations. (A) Linear stability analysis of Eq. 1 distinguishes three different regions in Fourier space: Domains I and III are dissipative, whereas domain II represents active modes. The radius of the active shell II corresponds approximately to the inverse of characteristic pattern formation scale Λ . The bandwidth κ measures the ability of the active fluid component to concentrate power input in Fourier space. (B) Two examples of exact stationary bulk solutions of Eq. 1 realizing Beltrami vector fields of opposite helicity, obtained from Eq. 5 by combining modes of the same helicity located on one of the marginally stable gray surfaces in A. (C) Simulations with random initial condition spontaneously select one of two helicity branches. The histogram represents an average over 150 runs with random initial conditions, sampled over the statistically stationary state starting at time $t = 20\tau$ (dashed line). Simulation parameters: $\Lambda = 75 \mu\text{m}$, $U = 72 \mu\text{m/s}$, $\kappa_1 = 0.9/\Lambda$, $L = 8\Lambda$ (see also Fig. 2 and *Supporting Information* for larger simulations).

between helical \mathbf{k} modes and \mathbf{p} , \mathbf{q} modes, where $s_k, s_p, s_q \in \{\pm\}$ are the corresponding helicity indexes [overbars denote complex conjugates of $\mathbf{h}^{s_p} = \mathbf{h}^{s_p}(\mathbf{p})$, etc. (19)]. There are 2 degrees of freedom per wavevector and hence eight types of interactions for every triple $(\mathbf{k}, \mathbf{p}, \mathbf{q})$. As evident from Eq. 4, arbitrary superpositions of modes with identical wavenumber $p = q = k_*$ and same helicity index annihilate the advection term, because $s_p p - s_q q = 0$ in this case. Therefore, by choosing k_* to be a root of the polynomial $\xi(k)$, corresponding to the gray surfaces in Fig. 1A, we obtain exact stationary solutions

$$\mathbf{v}^\pm(\mathbf{x}) = \sum_{\mathbf{k}, k=k_*} u^\pm(\mathbf{k}) \mathbf{h}^\pm(\mathbf{k}) e^{i\mathbf{k}\cdot\mathbf{x}}, \quad [5]$$

where $u^\pm(-\mathbf{k}) = \bar{u}^\pm(\mathbf{k})$ ensures real-valued flow fields. In particular, these solutions (Eq. 5) correspond to Beltrami flows (43–45), obeying $\nabla \wedge \mathbf{v}^\pm = \pm k_* \mathbf{v}^\pm$. Applying the parity operator to any right-handed solution $\mathbf{v}^+(\mathbf{x})$ generates the corresponding left-handed solution $\mathbf{v}^-(\mathbf{x})$ and vice versa (Fig. 1B).

Although the exact solutions $\mathbf{v}^\pm(\mathbf{x})$ describe stationary Beltrami fields (43–45) of fixed total helicity $\mathcal{H}^\pm = \int d^3x \mathbf{v}^\pm \cdot \boldsymbol{\omega}^\pm$, where $\boldsymbol{\omega} = \nabla \wedge \mathbf{v}$ is the vorticity, it is not yet clear whether parity violation is a generic feature of arbitrary time-dependent solutions of Eq. 1. As we demonstrate next, simulations with random initial conditions do indeed converge to statistically stationary flow states that spontaneously break mirror symmetry and are close to Beltrami flows.

Spontaneous Mirror-Symmetry Breaking in Time-Dependent Solutions. We simulate the full nonlinear Eq. 1 on a periodic cubic domain (size L) using a spectral algorithm (Numerical Methods). Simulations are performed for typical bacterial parameters ($\Gamma_0, \Gamma_2, \Gamma_4$), keeping the vortex scale $\Lambda = 75 \mu\text{m}$ and circulation speed $U = 72 \mu\text{m/s}$ fixed (34, 35) and comparing three spectral bandwidths $\kappa_S = 0.63/\Lambda = 8.4 \text{ mm}^{-1}$, $\kappa_I = 0.90/\Lambda = 12 \text{ mm}^{-1}$, and $\kappa_W = 2.11/\Lambda = 28.1 \text{ mm}^{-1}$, corresponding to active fluids with a small (S), an intermediate (I), and a wide (W) range of energy injection scales. A small bandwidth means that the active stresses inject energy into a narrow shell in Fourier space, whereas a wide bandwidth means energy is pumped into a wide range of Fourier modes (Fig. 1A). All simulations are initiated with weak incompressible random flow fields. For all three values of κ , we observe spontaneous mirror-symmetry breaking indicated by the time evolution of the mean helicity $H = (1/L^3) \int d^3x h$, where $h = \mathbf{v} \cdot \boldsymbol{\omega}$ is the local helicity. During the initial relaxation phase, the flow dynamics are attracted to states of well-defined total helicity and remain in such a statistically stationary configuration for the rest of the simulation. As

an illustration, Fig. 1C shows results from 150 runs for $\kappa = \kappa_I$ and $L = 8\Lambda$, with flow settling into a positive (negative) mean helicity state 72 (78) times. This spontaneous mirror-symmetry breaking is robust against variations of the bandwidth and simulation box size, as evident from the local vorticity and helicity fields for $\kappa = \kappa_S$ and $L = 32\Lambda$ in Fig. 2A and B.

Beltrami-Flow Attractors. Having confirmed spontaneous parity violation for the time-dependent solutions of Eq. 1, we next characterize the chaotic flow attractors. To this end, we measure and compare the histograms of the angles between the local velocity field $\mathbf{v}(t, \mathbf{x})$ and vorticity field $\boldsymbol{\omega}(t, \mathbf{x})$ for the three bandwidths $\kappa_S < \kappa_I < \kappa_W$. Our numerical results reveal that a smaller active bandwidth, corresponding to a more sharply defined scale selection, causes a stronger alignment of the two fields (Fig. 2C). Recalling that perfect alignment, described by $\boldsymbol{\omega} = \lambda \mathbf{v}$ with eigenvalue λ , is the defining feature of Beltrami flows (43–45), we introduce the Beltrami measure $\beta = \mathbf{v} \cdot \boldsymbol{\omega} / (\lambda |\mathbf{v}|^2)$. For ideal Beltrami fields, the distribution of β becomes a delta peak centered at $\beta = 1$. Identifying λ with the midpoint of the active shell ($\lambda \approx \pi/\Lambda$), which approximately corresponds to the most dominant pattern formation scale in Eq. 1, we indeed find that the numerically computed flow fields exhibit β distributions that are sharply peaked at $\beta = 1$ (Fig. 2D). Keeping Λ and U constant, the sharpness of the peak increases with decreasing active bandwidth κ . These results imply that active fluids with well-defined intrinsic scale selection realize flow structures that are statistically close to Beltrami fields, as suggested by the particular analytical solutions derived earlier.

Discussion

Spontaneous Parity Breaking vs. Surgical Mode Removal. Important previous studies identified bifurcation mechanisms (66–68) leading to parity violation in 1D and 2D (69) continuum models of pattern-forming nonequilibrium systems (70, 71). The above analytical and numerical results generalize these ideas to 3D fluid flows, by showing that an active scale selection mechanism can induce spontaneous helical mirror-symmetry breaking. Such self-organized parity violation can profoundly affect energy transport and mixing in 3D active fluids, which do not satisfy the premises of Kraichnan’s thermodynamic no-go argument (23). An insightful recent study (24), based on the classical Navier–Stokes equation, found that an ad hoc projection of solutions to positive or negative helicity subspaces can result in an inverse cascade but it has remained an open question whether such a surgical mode removal can be realized experimentally in passive fluids. By contrast, active fluids spontaneously achieve helical parity breaking (Fig. 1C) by approaching Beltrami-flow states

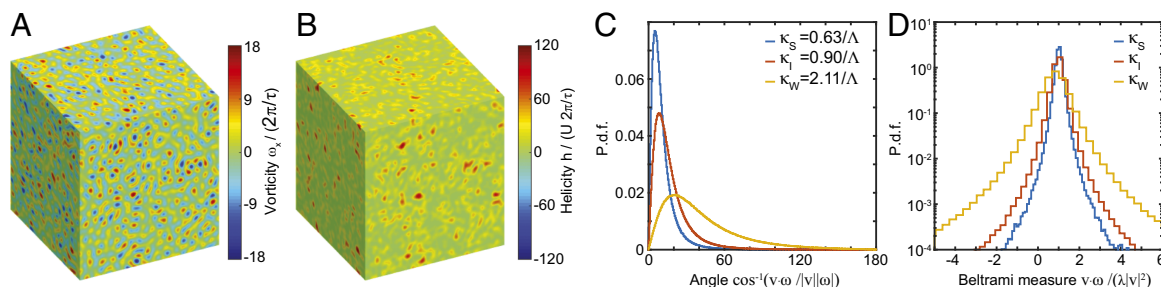


Fig. 2. Active fluids spontaneously break mirror symmetry by realizing Beltrami-type flows. (A) Snapshot of a representative vorticity component field ω_x (Movie S1) for an active fluid with small bandwidth $\kappa_S = 0.63/\Lambda$, as defined in Fig. 1A. (B) The corresponding helicity field signals parity-symmetry breaking, leading to a positive-helicity flow in this example. (C) Histograms of the angles between velocity \mathbf{v} and vorticity $\boldsymbol{\omega}$ quantify the alignment between the two fields for different active bandwidths $\kappa_S < \kappa_I < \kappa_W$: The smaller the bandwidth is, the stronger the alignment between \mathbf{v} and $\boldsymbol{\omega}$. (D) Numerically estimated distributions of the Beltrami measure, $\beta = \mathbf{v} \cdot \boldsymbol{\omega} / (\lambda |\mathbf{v}|^2)$, shown on a log scale. An ideal Beltrami flow with $\boldsymbol{\omega} = \lambda \mathbf{v}$ produces a delta peak centered at $\beta = 1$. Identifying λ with the midpoint of the active shell ($\lambda \approx \pi/\Lambda$), which approximately corresponds to the most unstable wavenumber and the characteristic pattern formation scale, we observe that a smaller active bandwidth leads to a sharper peak and hence more Beltrami-like flows. Data were taken at a single representative time point long after the characteristic relaxation time. Simulation parameters: $\Lambda = 75 \mu\text{m}$, $U = 72 \mu\text{m/s}$, $L = 32\Lambda$.

(Fig. 2 C and D), suggesting the possibility of a self-organized inverse energy cascade even in 3D. Before testing this hypothesis we recall that the model defined by Eq. 1 merely assumes the existence of linear active stresses to account for pattern scale selection as observed in a wide range of microbial suspensions (35, 38, 54, 72), but does not introduce nonlinearities beyond those already present in the classical Navier–Stokes equations. That is, energy redistribution in the solvent fluid is governed by the advective nonlinearities as in conventional passive liquids.

Inverse Cascade in 3D Active Fluids. To quantify how pattern scale selection controls parity breaking and energy transport in active fluids, we analyzed large-scale simulations ($L = 32\Lambda$; Fig. 2A and B) for different values of the activity bandwidth κ (Fig. 1A) while keeping the pattern scale Λ and the circulation speed U fixed. The active shell (red domain II in Fig. 1A) corresponds to the energy injection range in Fourier space and provides a natural separation between large flow scales (blue domain I) and small flow scales (blue domain III). Consequently, the forward cascade corresponds to a net energy flux from domain II to domain III, whereas an inverse cascade transports energy from domain II to I. We calculate energy spectra $e(k) = e^+(k) + e^-(k)$ and energy fluxes $\Pi(k) = \Pi^+(k) + \Pi^-(k)$ directly from our simulation data, by decomposing the velocity field into helical modes as in Eq. 2, which yields a natural splitting into cumulative energy

and flux contributions $e^\pm(k)$ and $\Pi^\pm(k)$ from helical modes $u^\pm(k)$ lying on the wavenumber shell $|\mathbf{k}| = k$ (Numerical Methods). Time-averaged spectra and fluxes are computed for each simulation run after the system has relaxed to a statistically stationary state (Fig. S2). For a small injection bandwidth κ_S , the energy spectra $e^\pm(k)$ reflect the broken mirror symmetry, with most of the energy being stored in either the positive-helicity or the negative-helicity modes (Fig. 3A), depending on the initial conditions. Moreover, in addition to the expected 3D forward transfer, the simulation data for κ_S also show a significant inverse transfer, signaled by the negative values of the total flux $\Pi(k)$ (yellow curve in Fig. 3B) in domain I. As evident from the blue curves in Fig. 3A and B, this inverse cascade is facilitated by the helical modes that carry most of the energy. For a large injection bandwidth $\kappa_W \gg \kappa_S$, the energy spectra continue to show signatures of helical symmetry breaking (Fig. 3E), but the energy transported to larger scales becomes negligible relative to the forward cascade, as contributions from opposite-helicity modes approximately cancel in the long-wavelength domain I (Fig. 3F). Results for the intermediate case κ_M still show a significant inverse transfer (Figs. S3 and S4E), demonstrating how the activity bandwidth—or, equivalently, the pattern selection range—controls both parity violation and inverse cascade formation in an active fluid. The upward transfer is noninertial at intermediate scales, as indicated by the wavenumber dependence of

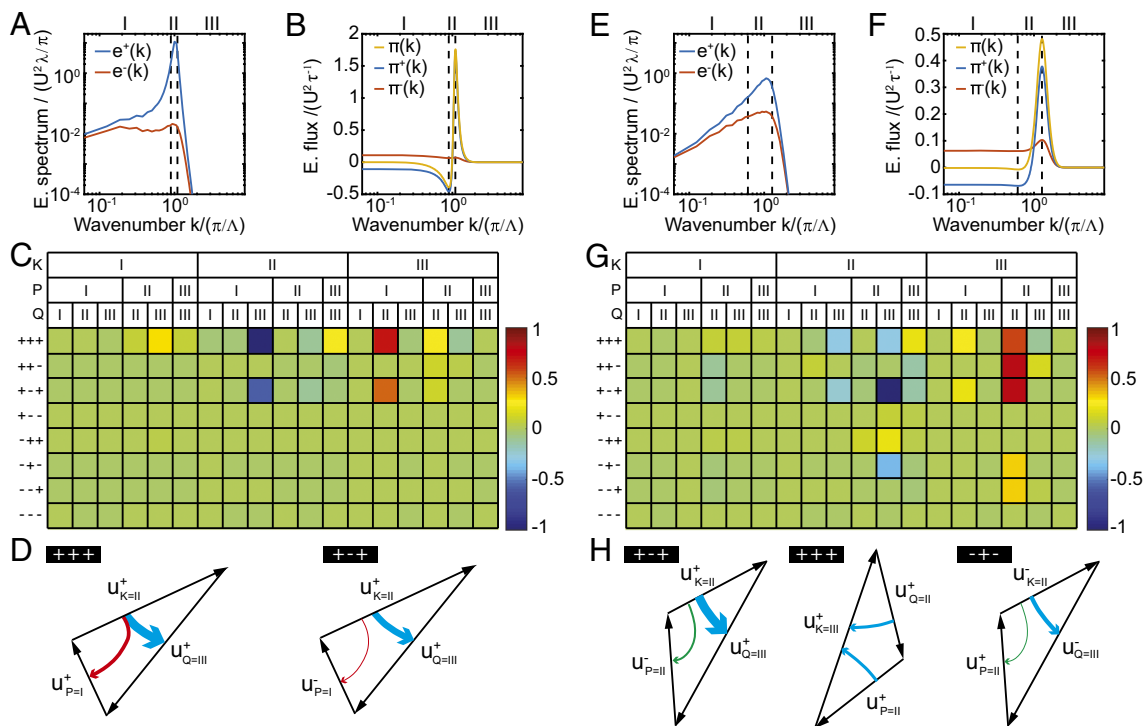


Fig. 3. Scale selection controls mirror-symmetry breaking and induces an inverse energy cascade. We demonstrate these effects for active fluids with (A–D) a small active bandwidth κ_S and (E–H) a wide bandwidth κ_W (Fig. 1A). The intermediate case κ_I is presented in Fig. S3. (A) Energy spectra $e^\pm(k)$ of the helical velocity-field modes show strong symmetry breaking for small bandwidth parameter κ_S . In this example, the system spontaneously selects positive helicity modes, such that $e^+(k) > e^-(k)$ at all dominant wavenumbers. Dashed vertical lines indicate the boundaries of the energy injection domain II. (B) The resulting energy fluxes $\Pi^\pm(k)$ combine into the total flux $\Pi(k)$, which is negative in region I and positive in region III, signaling inverse and forward energy transfers, respectively. (C) Contributions to the energy flow $\langle \mathcal{T}_{KPO}^{K^*P^*Q^*} \rangle$ between the three spectral domains I, II, and III (18 possibilities, columns) from the eight types of triad interactions (rows). In reflection-invariant turbulence, this table remains unchanged under upside-down flipping ($+\leftrightarrow-$). Instead, we observe a strong asymmetry, with two cumulative triads (D) dominating the energy transfer. Red and blue arrows represent transfer toward large and small scales, respectively, and thickness represents magnitude of energy flow. Green arrows (H) represent transfer within the same spectral domain. The direction of the energy flow is in agreement with the instability assumption of Waleffe (19). In this case, 18.2% of the injected energy is transferred from region II to region I and 81.8% is transferred from region II to III. (E–H) The same plots for an active fluid with wide active bandwidth κ_W . (E and F) Energy spectra show weaker parity breaking (E) and suppression of the inverse energy cascade (F). (G) The energy flow table partially recovers the upside-down ($+\leftrightarrow-$) symmetry. (H) The most active triads now favor the forward cascade, so that only 1.1% of the injected energy flows into region I, whereas 98.9% is transferred into region III. Data represent averages over single runs (Fig. S2). Simulation parameters are identical to those in Fig. 2.

the energy flux (Fig. 3B). At very large scales $\gg \Lambda$, however, the flux approaches an inertial plateau (*Cascade Characteristics*). In contrast to the energy-mediated 2D inverse cascade in passive fluids, the helicity-driven 3D inverse cascade in active fluids is linked to the formation of extended vortex chain complexes that move collectively through the fluid (*Movie S1* and *Cascade Characteristics*).

Triad Interactions. Our numerical flux measurements confirm directly the existence of a self-sustained 3D inverse cascade induced by spontaneous parity violation, consistent with earlier projection-based arguments for the classical Navier–Stokes equations (24). An inverse energy cascade can exist in 3D active fluids because mirror-symmetry breaking favors only a subclass of all possible triad interactions, which describe advective energy transfer in Fourier space between velocity modes $\{v(\mathbf{k}), v(\mathbf{p}), v(\mathbf{q})\}$ with $\mathbf{k} + \mathbf{p} + \mathbf{q} = 0$ (compare with Eq. 4). To analyze in detail which triads are spontaneously activated in a pattern-forming nonequilibrium fluid, we consider combinations $K, P, Q \in \{I, II, III\}$ of the spectral domains in Fig. 1A and distinguish modes by their helicity index $s_K, s_P, s_Q \in \{\pm\}$. The helicity-resolved integrated energy flow into the region (K, s_K) due to interaction with regions (P, s_P) and (Q, s_Q) is given by (*Numerical Methods*)

$$\mathcal{T}_{K P Q}^{s_K s_P s_Q} = \frac{1}{2} (\tilde{\mathcal{T}}_{K P Q}^{s_K s_P s_Q} + \tilde{\mathcal{T}}_{K Q P}^{s_K s_Q s_P}), \quad [6]$$

where the unsymmetrized flows are defined by

$$\tilde{\mathcal{T}}_{K P Q}^{s_K s_P s_Q} = - \int d^3 x v_K^{s_K} \cdot [(v_P^{s_P} \cdot \nabla) v_Q^{s_Q}], \quad [7]$$

with $v_K^{s_K}(t, \mathbf{x})$ denoting the helical Littlewood–Paley velocity components, obtained by projecting on modes of a given helicity index $s_K \in \{\pm\}$ restricted to the Fourier domain K . Entries of \mathcal{T} are large when the corresponding triads are dominant.

For active fluids, Fourier space is naturally partitioned into three regions (Fig. 1A) and there are $2^3 = 8$ helicity index combinations. The triad tensor \mathcal{T} is symmetric in the last two indexes, so that \mathcal{T} has 8×18 independent components encoding the fine structure of the advective energy transport. Stationary time averages for $\langle \mathcal{T} \rangle$, measured from our simulations (*Numerical Methods*) for small (κ_S) and wide (κ_W) energy injection bandwidths, are shown in Fig. 3C and G. For reflection-symmetric turbulent flows, these two tables would remain unchanged under an upside-down flip ($+\leftrightarrow-$). By contrast, we find a strong asymmetry for a narrow bandwidth κ_S (Fig. 3C), which persists in weakened form for κ_W (Fig. 3G). Specifically, we observe for κ_S two dominant cumulative triads with energy flowing out of the active spectral range II into the two passive domains I and III (Fig. 3D). These cumulative triads visualize dominant entries of the tables in Fig. 3C and G and represent the total contributions from all triadic interactions between modes with given helicity indexes and with “legs” lying in the specified spectral domain. The observed energy transfer directions, with energy flowing out of the intermediate domain II when the small-scale modes carry the same helicity index, are in agreement with a turbulent instability mechanism proposed by Waleffe (19). Interestingly, however, our numerical results show that both “R”-interaction channels $+++$ and $+-+$ contribute substantially even in the case of

strong parity breaking (κ_S ; Fig. 3D); when one surgically projects the full dynamics onto states with fixed parity, only the $+++$ channel remains (24). By contrast, for a wide bandwidth κ_W , the dominating triad interactions (Fig. 3H) favor the forward cascade. Hence, the inverse energy cascade in 3D active fluids is possible because only a subset of triadic interactions is active in the presence of strong mirror-symmetry breaking. This phenomenon is controlled by the spectral bandwidth of the scale selection mechanism.

Enhanced Mixing. Eq. 1 describe a 3D isotropic fluid capable of transporting energy from smaller to larger scales. Previously, self-organized inverse cascades were demonstrated only in effectively 2D flows (6, 18, 20, 25, 73–79). The 2D inverse cascade has been intensely studied in meteorology (6, 7), a prominent example being Jovian atmospheric dynamics (80), because of its importance for the mixing of thin fluid layers (81–83). Analogously, the 3D inverse cascade and the underlying Beltrami-flow structure are expected to enhance mixing and transport in active fluids. Arnold (43) showed that steady solutions of the incompressible Euler equations include Beltrami-type ABC flows (44) characterized by chaotic streamlines. Similarly, the Beltrami structure of the active-flow attractors of Eq. 1 implies enhanced local mixing. Combined with the presence of an inverse cascade, which facilitates additional large-scale mixing through the excitation of long-wavelength modes, these results suggest that active biological fluids, such as microbial suspensions (35, 54, 72), can be more efficient at stirring fluids and transporting nutrients than previously thought.

Conclusions

To detect Beltrami flows in biological or engineered active fluids, one has to construct histograms and spectra as shown in Figs. 2C and D and 3A and E from experimental fluid velocity and helicity data, which is possible with current fluorescence imaging techniques (13, 35). Moreover, helical tracer particles (84) can help distinguish left-handed and right-handed flows. The above analysis predicts that Beltrami-flow structures, mirror-symmetry breaking, and the inverse 3D cascade appear more pronounced when the pattern selection is focused in a narrow spectral range. Our simulations further suggest that the relaxation time required for completion of the mirror-symmetry breaking process depends on the domain size (Fig. S5). For small systems, the relaxation is exponentially fast, whereas for large domains relaxation proceeds in two stages, first exponentially and then linearly. In practice, it may therefore be advisable to accelerate relaxation by starting experiments from rotating initial conditions.

Methods

Eq. 1 was solved numerically in the vorticity-vector potential form with periodic boundary conditions using a spectral code with 3/2 anti-aliasing (*Numerical Methods*). Tables in Fig. 3 were calculated using the Littlewood–Paley decomposition and collocation.

ACKNOWLEDGMENTS. We thank Aden Forrow, Francis Woodhouse, Luca Biferale, Moritz Linkmann, and Michael Tribelsky for helpful discussions.

1. Frisch U (2004) *Turbulence* (Cambridge Univ Press, Cambridge, UK).
2. McComb WD (1990) *The Physics of Fluid Turbulence* (Oxford Science Publications, New York).
3. Higdon JC (1984) Density fluctuations in the interstellar medium: Evidence for anisotropic magnetogasdynamic turbulence. I - Model and astrophysical sites. *Astrophys J* 285:109–123.
4. Federrath C, Roman-Duval J, Klessen RS, Schmidt W, Mac Low M-M (2010) Comparing the statistics of interstellar turbulence in simulations and observations—Solenoidal versus compressive turbulence forcing. *Astron Astrophys* 512:A81.
5. Bruno R, Carbone V (2013) The solar wind as a turbulence laboratory. *Living Rev Solar Phys* 10(2013):2.
6. Nastrom GD, Gage KS, Jasperson WH (1984) Kinetic energy spectrum of large- and mesoscale atmospheric processes. *Nature* 310:36–38.

7. Lindborg E (1999) Can the atmospheric kinetic energy spectrum be explained by two-dimensional turbulence? *J Fluid Mech* 388:259–288.
8. Thorpe S (2005) *The Turbulent Ocean* (Cambridge Univ Press, Cambridge, UK).
9. Enriquez RM, Taylor JR (2015) Numerical simulations of the competition between wind-driven mixing and surface heating in triggering spring phytoplankton blooms. *ICES J Mar Sci* 72(6):1926–1941.
10. Taylor JR, Stocker R (2012) Trade-offs of chemotactic foraging in turbulent water. *Science* 338(6107):675–679.
11. Noullez A, Wallace G, Lempert W, Miles RB, Frisch U (1997) Transverse velocity increments in turbulent flow using the RELIEF technique. *J Fluid Mech* 339:287–307.
12. Nieuw GS, Swinney HL (1999) Velocity structure functions, scaling, and transitions in high-Reynolds-number Couette-Taylor flow. *Phys Rev E* 59(5):5457–5467.

13. Xu H, Bourgoin M, Ouellette NT, Bodenschatz E (2006) High order Lagrangian velocity statistics in turbulence. *Phys Rev Lett* 96:024503.
14. Kolmogorov AN (1941) The local structure of turbulence in incompressible viscous fluid for very large Reynolds numbers. *Dokl Akad Nauk SSSR* 30:301–305.
15. Kolmogorov AN (1941) On degeneration (decay) of isotropic turbulence in an incompressible viscous liquid. *Dokl Akad Nauk SSSR* 31:538–540.
16. Kolmogorov AN (1941) Dissipation of energy in locally isotropic turbulence. *Dokl Akad Nauk SSSR* 32:16–18.
17. Kraichnan RH (1967) Inertial ranges in two-dimensional turbulence. *Phys Fluids* 10(7):1417–1423.
18. Kraichnan RH, Montgomery D (1980) Two-dimensional turbulence. *Rep Prog Phys* 43:547–619.
19. Waleffe F (1992) The nature of triad interactions in homogeneous turbulence. *Phys Fluids A* 4(2):350–363.
20. Kellay H, Goldburg WI (2002) Two-dimensional turbulence: A review of some recent experiments. *Rep Prog Phys* 65:845–894.
21. Pumir A, Xu H, Bodenschatz E, Grauer R (2016) Single-particle motion and vortex stretching in three-dimensional turbulent flows. *Phys Rev Lett* 116:124502.
22. Fefferman CL (2012) Existence and smoothness of Navier-Stokes equations. Available at www.claymath.org/millennium-problems/navier-stokes-equation. Accessed January 24, 2017.
23. Kraichnan RH (1973) Helical turbulence and absolute equilibrium. *J Fluid Mech* 59(4):745–752.
24. Biferale L, Musacchio S, Toschi F (2012) Inverse energy cascade in three-dimensional isotropic turbulence. *Phys Rev Lett* 108(16):164501.
25. Boffetta G, Ecke RE (2012) Two-dimensional turbulence. *Annu Rev Fluid Mech* 44(1):427–451.
26. Danilov SD, Gurarie D (2000) Quasi-two-dimensional turbulence. *Phys Usp* 170:921–968.
27. Moffatt HK (1969) The degree of knottedness of tangled vortex lines. *J Fluid Mech* 35(1):117–129.
28. Wu CS, Ambler E, Hayward RW, Hoppes DD, Hudson RP (1957) Experimental test of parity conservation in beta decay. *Phys Rev* 105:1413–1415.
29. Watson JD, Crick FHC (1953) Molecular structure of nucleic acids: A structure for deoxyribose nucleic acid. *Nature* 171:737–738.
30. Armon S, Efrati E, Kupferman R, Sharon E (2011) Geometry and mechanics in the opening of chiral seed pods. *Science* 333(6050):1726–1730.
31. Woodhouse FG, Goldstein RE (2012) Spontaneous circulation of confined active suspensions. *Phys Rev Lett* 109(16):168105.
32. Wioland H, Woodhouse FG, Dunkel J, Kessler JO, Goldstein RE (2013) Confinement stabilizes a bacterial suspension into a spiral vortex. *Phys Rev Lett* 110(26):268102.
33. Wioland H, Woodhouse FG, Dunkel J, Goldstein RE (2016) Ferromagnetic and antiferromagnetic order in bacterial vortex lattices. *Nat Phys* 12(4):341–345.
34. Sokolov A, Aranson IS (2012) Physical properties of collective motion in suspensions of bacteria. *Phys Rev Lett* 109:248109.
35. Dunkel J, et al. (2013) Fluid dynamics of bacterial turbulence. *Phys Rev Lett* 110(22):228102.
36. Slomka J, Dunkel J (2015) Generalized Navier-Stokes equations for active suspensions. *EPJ ST* 224:1349–1358.
37. Slomka J, Dunkel J (2016) Geometry-dependent viscosity reduction in sheared active fluids. [arXiv:1608.01757](https://arxiv.org/abs/1608.01757).
38. Sanchez J, Chen DTN, DeCamp SJ, Heymann M, Dogic Z (2012) Spontaneous motion in hierarchically assembled active matter. *Nature* 491:431–434.
39. Giomi L (2015) Geometry and topology of turbulence in active nematics. *Phys Rev X* 5:031003.
40. Bricard A, Caussin J-B, Desreumaux N, Dauchot O, Bartolo D (2013) Emergence of macroscopic directed motion in populations of motile colloids. *Nature* 503:95–98.
41. Walthar A, Muller AHE (2008) Janus particles. *Soft Matter* 4:663–668.
42. Thutupalli S, Seemann R, Herminghaus S (2011) Swarming behavior of simple model squirmers. *New J Phys* 13(7):073021.
43. Arnold VI (1965) Sur la topologie des écoulements stationnaires des fluides parfaits. *C R Acad Sci Paris* 261:17–20.
44. Dombre T, et al. (1986) Chaotic streamlines in the ABC flows. *J Fluid Mech* 167:353–391.
45. Etnyre J, Ghrist R (2000) Contact topology and hydrodynamics: I. Beltrami fields and the Seifert conjecture. *Nonlinearity* 13(2):441–458.
46. Jiang H-R, Yoshinaga N, Sano M (2010) Active motion of a Janus particle by self-thermophoresis in a defocused laser beam. *Phys Rev Lett* 105:268302.
47. Buttinoni I, et al. (2013) Dynamical clustering and phase separation in suspensions of self-propelled colloidal particles. *Phys Rev Lett* 110:238301.
48. Wensink HH, et al. (2012) Meso-scale turbulence in living fluids. *Proc Natl Acad Sci USA* 109(36):14308–14313.
49. Bratanov V, Jenko F, Frey E (2015) New class of turbulence in active fluids. *Proc Natl Acad Sci USA* 112(49):15048–15053.
50. Simha RA, Ramaswamy S (2002) Hydrodynamic fluctuations and instabilities in ordered suspensions of self-propelled particles. *Phys Rev Lett* 89(5):058101.
51. Saintillan D, Shelley M (2008) Instabilities, pattern formation and mixing in active suspensions. *Phys Fluids* 20:123304.
52. Marchetti MC, et al. (2013) Hydrodynamics of soft active matter. *Rev Mod Phys* 85:1143–1189.
53. Ravnik M, Yeomans JM (2013) Confined active nematic flow in cylindrical capillaries. *Phys Rev Lett* 110:026001.
54. Dombrowski C, Cisneros L, Chatkaew S, Goldstein RE, Kessler JO (2004) Self-concentration and large-scale coherence in bacterial dynamics. *Phys Rev Lett* 93(9):098103.
55. Cisneros LH, Cortez R, Dombrowski C, Goldstein RE, Kessler JO (2007) Fluid dynamics of self-propelled micro-organisms, from individuals to concentrated populations. *Exp Fluids* 43:737–753.
56. Bellouta H, Bloom F (2014) Incompressible bipolar and non-Newtonian viscous fluid flow. *Advances in Mathematical Fluid Mechanics* (Springer, Basel).
57. Ma Y-P, Spiegel EA (2011) A diagrammatic derivation of (convective) pattern equations. *Physica D* 240:150–165.
58. Beresnev IA, Nikolaevskiy VN (1993) A model for nonlinear seismic waves in a medium with instability. *Physica D* 66:1–6.
59. Tribelsky MI, Tsuboi K (1996) New scenario for transition to turbulence? *Phys Rev Lett* 76:1631–1634.
60. Tribelsky MI (2008) Patterns in dissipative systems with weakly broken continuous symmetry. *Phys Rev E* 77:035202.
61. Ouellette NT, Gollub JP (2008) Dynamic topology in spatiotemporal chaos. *Phys Fluids* 20(6):064104.
62. Varshney A, et al. (2016) Multi-scale flow in a microscale oil-in-oil emulsion. *Soft Matter* 12:1759–1764.
63. Bregulla AP, Yang H, Cichos F (2014) Stochastic localization of microswimmers by photon nudging. *ACS Nano* 8(7):6542–6550.
64. Fedosov DA, Sengupta A, Gompper G (2015) Effect of fluid–colloid interactions on the mobility of a thermophoretic microswimmer in non-ideal fluids. *Soft Matter* 11:6703–6715.
65. Kümmel F, et al. (2013) Circular motion of asymmetric self-propelling particles. *Phys Rev Lett* 110(19):198302.
66. Malomed BA, Tribelsky MI (1984) Bifurcations in distributed kinetic systems with aperiodic instability. *Physica D* 14(1):67–87.
67. Couillet P, Goldstein RE, Gunaratne GH (1989) Parity-breaking transitions of modulated patterns in hydrodynamic systems. *Phys Rev Lett* 63(18):1954–1957.
68. Knobloch E, Hettel J, Dangelmayr G (1995) Parity breaking bifurcation in inhomogeneous systems. *Phys Rev Lett* 74:4839–4842.
69. Fujisaka H, Honkawa T, Yamada T (2003) Amplitude equation of higher-dimensional Nikolaevskii turbulence. *Prog Theor Phys* 109(6):911–918.
70. Goldstein RE, Gunaratne GH, Gil L, Couillet P (1991) Hydrodynamic and interfacial patterns with broken space-time symmetry. *Phys Rev A* 43:6700–6721.
71. Tribelsky MI (1997) Short-wavelength instability and transition to chaos in distributed systems with additional symmetry. *Phys Usp* 40(2):159–180.
72. Sokolov A, Aranson IS, Kessler JO, Goldstein RE (2007) Concentration dependence of the collective dynamics of swimming bacteria. *Phys Rev Lett* 98:158102.
73. Smith LM, Chasnov JR, Waleffe F (1996) Crossover from two- to three-dimensional turbulence. *Phys Rev Lett* 77(12):2467–2470.
74. Smith LM, Waleffe F (1999) Transfer of energy to two-dimensional large scales in forced, rotating three-dimensional turbulence. *Phys Fluids* 11:1608–1622.
75. Smith LM, Waleffe F (2002) Generation of slow large scales in forced rotating stratified turbulence. *J Fluid Mech* 451:145–168.
76. Xia H, Punzmann H, Falkovich G, Shats MG (2008) Turbulence-condensate interaction in two dimensions. *Phys Rev Lett* 101(19):194504.
77. Mininni PD, Alexakis A, Pouquet A (2009) Scale interactions and scaling laws in rotating flows at moderate Rossby numbers and large Reynolds numbers. *Phys Fluids* 21(1):015108.
78. Celani A, Musacchio S, Vincenzi D (2010) Turbulence in more than two and less than three dimensions. *Phys Rev Lett* 104(18):184506.
79. Xia H, Byrne D, Falkovich G, Shats M (2011) Upscale energy transfer in thick turbulent fluid layers. *Nat Phys* 7(4):321–324.
80. Vasavada AR, Showman AP (2005) Jovian atmospheric dynamics: An update after Galileo and Cassini. *Rep Prog Phys* 68:1935–1996.
81. Rutgers MA (1998) Forced 2D turbulence: Experimental evidence of simultaneous inverse energy and forward enstrophy cascades. *Phys Rev Lett* 81:2244–2247.
82. Bernard D, Boffetta G, Celani A, Falkovich G (2007) Inverse turbulent cascades and conformally invariant curves. *Phys Rev Lett* 98:024501.
83. Bernard D, Boffetta G, Celani A, Falkovich G (2006) Conformal invariance in two-dimensional turbulence. *Nat Phys* 2(2):124–128.
84. Gustavsson K, Biferale L (2016) Preferential sampling of helicity by isotropic helicoids. *Phys Rev Fluids* 1:054201.
85. Canuto C, Hussaini MY, Quarteroni A, Zang TA (1988) *Spectral Methods in Fluid Dynamics* (Springer, Berlin).
86. Schwarz G (1995) *Hodge Decomposition—A Method for Solving Boundary Value Problems*, Lecture Notes in Mathematics (Springer, Berlin), Vol 1607.
87. Ascher UM, Ruuth SJ, Wetton BTR (1995) Implicit-explicit methods for time-dependent partial differential equations. *SIAM J Numer Anal* 32(3):797–823.
88. Heidenreich S, Dunkel J, Klapp SHL, Bär M (2016) Hydrodynamic length-scale selection in microswimmer suspensions. *Phys Rev E* 94:020601(R).
89. Purcell EM (1977) Life at low Reynolds number. *Am J Phys* 45(1):3–11.
90. Sokolov A, Aranson IS (2009) Reduction of viscosity in suspension of swimming bacteria. *Phys Rev Lett* 103:148101.
91. López HM, Gachelin J, Douarache C, Auradou H, Clément E (2015) Turning bacteria suspensions into superfluids. *Phys Rev Lett* 115:028301.
92. Ramaswamy S (2010) The mechanics and statistics of active matter. *Annu Rev Cond Mat Phys* 1:323–345.
93. Drescher K, Goldstein RE, Michel N, Polin M, Tuval I (2010) Direct measurement of the flow field around swimming microorganisms. *Phys Rev Lett* 105:168101.
94. Drescher K, Dunkel J, Cisneros LH, Ganguly S, Goldstein RE (2011) Fluid dynamics and noise in bacterial cell-cell and cell-surface scattering. *Proc Natl Acad Sci USA* 108(27):10940–10945.

Supporting Information

Supporting Information Corrected Mar 10, 2017

Słomka and Dunkel 10.1073/pnas.1614721114

Comparison with Experiments

The generalized Navier–Stokes equations defined in Eq. 1 of the main text aim to provide an effective three-parameter description of solvent flows driven by an active component. Although the flow structures seen in the simulations look visually similar to those observed in experiments on bacterial and other active suspensions, a quantitative comparison with experimental data is needed to evaluate the practical applicability of the theory.* To contribute toward closing the gap between theory and experiments, we performed systematic parameter scans, comparing fluid flow statistics measured in our simulations with recently reported experimental data for two different classes of active fluids: (i) concentrated quasi-3D suspensions of swimming *B. subtilis* bacteria (35) and (ii) ATP-driven microtubule networks (38). This analysis identified specific parameter values Γ_0 , Γ_2 , and Γ_4 for these two paradigmatic experimental systems, demonstrating in both cases good agreement between theory and available experimental data for velocity distributions and correlation functions (Fig. S1).

Bacterial Suspensions. The experiments reported in ref. 35 studied dense suspensions of rod-like *B. subtilis* bacteria swimming in a quasi-3D microfluidic channel (height ~ 80 μm , radius ~ 750 μm). The bacterial velocity field was reconstructed from bright-field microscopy videos using particle imaging velocimetry (PIV), and the solvent flow dynamics were measured by particle tracking velocimetry (PTV) using micrometer-sized fluorescent tracer beads. The experimental setup allowed the observation of 2D slices through the 3D velocity field, yielding data for the in-plane velocity components. From these 2D data, velocity distributions and correlation functions for bacteria and passive tracer particles were reconstructed, showing close correlations between bacterial dynamics and solvent flows. To compare the experimental measurements in ref. 35 with our 3D simulations, we mimicked the experimental setup by selecting arbitrary 2D planes in our 3D simulation volume. We then measured the in-plane velocity components and compared the numerically calculated velocity statistics with the corresponding experimental data (Fig. S1A–C).

Fig. S1A compares the experimentally measured velocity distribution for bacteria (open circles) and solvent tracer particles (solid circles) with the statistics of the five-parameter model for the bacterial velocity field considered in ref. 35 (black line labeled “theory”) and our generalized Navier–Stokes model (blue line). As discussed by the authors of ref. 35, their model for the bacterial dynamics fails to capture the tails of the velocity distributions as it includes an effective fourth-order velocity potential (representing steric alignment interactions) that dominates the tails of velocity distributions in their simulations. By contrast, our generalized Navier–Stokes model accurately captures the experimentally measured Gaussian velocity probability distribution functions (PDFs) over the whole range of the available experimental data (see Fig. S1C legend for a summary of fit parameters).

Fig. S1B compares the equal-time (in-plane) velocity correlation functions (VCFs) for the bacteria, tracer particles, and the theories. As mentioned in ref. 35, the VCFs for tracer par-

ticles become unreliable at large distances $r > 50$ μm , due to the deliberately low seeding densities of the tracer particles in these experiments. Low tracer densities were required to minimize feedback from passive tracers on the active suspension dynamics. This meant, however, that tracer particle pairs with large spatial separation r are significantly less frequently observed. Notwithstanding such experimental limitations, we find that the two complementary continuum models for bacterial and solvent flow yield qualitatively and quantitatively similar VCFs, correctly reflecting the typical vortex size ~ 50 – 70 μm in the negative part of the VCFs.

Fig. S1C compares the simulation results for the velocity auto-correlation functions (VACFs) with the corresponding experimental results at different bacterial activities (35) due to oxygen depletion. PTV-based VACFs were not given in ref. 35 as a specific tracer particle typically spends only a short time in the 2D field of view of the microscope before diffusing out of view. As evident from Fig. S1C, our generalized Navier–Stokes model can correctly reproduce the functional form of the PIV-based VACFs at high (green), intermediate (blue), and low (magenta) activities. With regard to a future quantitative characterization and classification of active fluids, we find it encouraging that a three-parameter model can account for the key velocity statistics reported in ref. 35.

Another interesting experimental observation reported but not rationalized in ref. 35 is the linear scaling of kinetic energy and enstrophy (figure 2d in ref. 35). We note that such a linear scaling is consistent with the Beltrami-like flows found in our simulations, which satisfy $v \propto \omega$ (Fig. 2C and D of the main text). Generally, we hope that the good agreement between the generalized Navier–Stokes model defined in Eqs. 1 of the main text and the experimental data for *B. subtilis* will stimulate additional 3D measurements on bacterial suspension in the near future, to test the Beltrami flow prediction directly and to explore the possibility of spontaneous mirror-symmetry breaking in detail.

ATP-Driven Microtubule Networks. The generalized Navier–Stokes equations defined in Eq. 1 of the main text merely assume that active stresses in an otherwise passive fluid lead to scale selection. They should therefore also apply to other types of active fluids, including ATP-driven microtubule suspensions. To test this hypothesis, we performed additional simulations to compare our model with experimental data published recently in ref. 38. The authors of this study report VCF data for tracer particles diffusing in fluid flows driven by predominantly extensile microtubule–kinesin bundles that form complex, approximately isotropic networks. The flows created by these active networks exhibit turbulent vortices on scales larger than the typical bundle-bending radii, suggesting that these flows are generated by the collective extensile dynamics of the bundles. Fig. S1D shows the experimental VCF data reported in ref. 38 (colored circles and lines) and a fit (black solid line) obtained from simulations of our generalized Navier–Stokes model, using the parameters specified in the legend.† Different ATP-controlled activity levels can be reproduced in our model through a trivial adjustment of the velocity scale U . Strikingly, changing the activity does not significantly alter the shape of the VCF after rescaling by kinetic energy for both bacterial and active microtubule suspensions (Fig. S1B

* We thank an anonymous reviewer for insisting on a detailed comparison with experiments. The comparison presented here benefited from the fact that one of us (J.D.) was involved in the original analysis of the experimental data in ref. 35.

† These parameters agree well with the typical velocity, length, and time scales expected from microbial suspensions.

and D), corroborating the idea that active suspensions can be robustly described by the leading-order terms of stress tensor expansions. More generally, the good agreement between the generalized Navier–Stokes model and two microscopically distinct active fluids supports the view that the main results and predictions of our study apply to a broad range of pattern-forming nonequilibrium fluids.

Model Justification

The generalized Navier–Stokes model defined in Eq. 1 of the main text describes the solvent flows in active suspensions through effective higher-order stresses that account phenomenologically for the experimentally observed flow-pattern scale selection (35, 38). By contrast, derivations of effective higher-order continuum models (88) often focus on the complementary problem of obtaining a higher-order equation for the orientational order-parameter fields of the active component by ignoring nonlinear inertial effects in the fluid. The generalized Navier–Stokes Eq. 1 in the main text avoid the latter oversimplification and assume a linear response between orientational order-parameter fields and ambient fluid (72).

Inertial Effects. The standard argument for neglecting inertial terms in the Navier–Stokes equations for dilute microbial suspensions is based on the typical length scale and swimming speed of a single bacterium and the viscosity of water (89). This argument is certainly correct for very low bacterial volume fractions when collective dynamical effects are negligible. The argument becomes invalid, however, at sufficiently high concentrations when collective effects dominate the suspension dynamics. There are three reasons for this: First, collective locomotion speeds of bacteria at moderate-to-high concentrations ($>5\%$ volume fraction) can be more than an order of magnitude larger than the self-propulsion speed of an individual bacterium (72). Second, the typical scale of a vortex is one or two magnitudes larger than the length of an individual cell (34, 35). Third, recent studies (90, 91) show that the collective dynamics can reduce the effective viscosity of a bacterial suspension by an order of magnitude. The combination of these three effects means that, in the collective swimming regime, the effective Reynolds number can approach 1 and, hence, inertial terms cannot a priori be neglected.

Active Stresses. At the fundamental continuum level, the fluid dynamics of a passive solvent are described by the Navier–Stokes equations. The effect of the active components on the fluid can be written as a collection of point forces entering on the right-hand side (rhs) of the Navier–Stokes equations. An important feature of intrinsically driven active suspensions (in contrast to externally forced colloidal suspensions) is given by the experimentally confirmed fact that bacteria and other microbes achieve locomotion through shape changes that require zero net force (89, 92–94). Considering, for instance, the simplest force dipole model, this means that forces can be paired, so that monopole contributions cancel and the leading-order contributions entering the Navier–Stokes equations take the form of divergences of stress tensors (92).

Slaving and Linear Response. In sufficiently dense suspensions, the net effective stress tensor depends on the collective dynamics, which are typically characterized through orientational order-parameter fields. If the fluid flows generated by the collective action of the active constituents dominate over their individual swimming dynamics, then one can assume that tensorial order parameters become “slaved” to the solvent dynamics. In this case, assuming a linear and isotropic response, one arrives at closure conditions for polar and nematic order parameters \mathbf{p} and \mathbf{Q} of the form

$$\mathbf{p} = \sum_{n=1}^{\infty} p_n \nabla^{2n} \mathbf{v}, \quad \mathbf{Q} = \sum_{n=1}^{\infty} q_n \nabla^{2n} (\nabla \mathbf{v})^+ \quad [\text{S1}]$$

where the superscript “+” denotes the traceless symmetric tensor part. Further assuming that the conventional viscous stresses and the active stresses are additive, that the leading active stresses are linear in the order parameters \mathbf{p} and \mathbf{Q} , and by truncating at order $n = 3$, one is led to a sixth-order stress tensor as in Eq. 1c of the main text. This reasoning can be formalized systematically through diagrammatic expansion techniques (57).[‡] The successful comparison with the experiments above suggests that such truncated stress tensors can capture essential aspects of the collective dynamics.

Numerical Methods

Numerical simulations were performed using a Fourier spectral method with a 3/2 rule to avoid aliasing when calculating the advection term through collocation (85). We typically used grids of size 243^3 . Larger resolutions are not necessary, because the highest-order term in Eq. 1 provides strong damping $\sim k^6$ at large wavenumbers k . We find solutions to Eq. 1 by using the Hodge decomposition (86) and solving the corresponding vorticity-vector potential problem

$$\partial_t \boldsymbol{\omega} + \nabla \wedge (\boldsymbol{\omega} \wedge \mathbf{v}) = \Gamma_0 \nabla^2 \boldsymbol{\omega} - \Gamma_2 \nabla^4 \boldsymbol{\omega} + \Gamma_4 \nabla^6 \boldsymbol{\omega}, \quad [\text{S2a}]$$

$$\nabla^2 \boldsymbol{\psi} = -\boldsymbol{\omega}, \quad [\text{S2b}]$$

where $\boldsymbol{\omega} = \nabla \wedge \mathbf{v}$ is the vorticity and $\boldsymbol{\psi}$ is the divergence-free vector potential related to the velocity field through $\mathbf{v} = \nabla \wedge \boldsymbol{\psi}$. Eq. S2 are evolved in time, using a third-order semiimplicit backward differentiation time-stepping scheme (86), calculating the nonlinear advection term explicitly while inverting the linear part implicitly. The discretized Eq. S2 maintain $\boldsymbol{\omega}$ and $\boldsymbol{\psi}$ divergence-free in exact arithmetic. To avoid slow buildup of nonzero divergence when working in double-precision arithmetic, numerical solutions are projected onto the divergence-free manifold during the time stepping. To calculate the energy transfer tables in Fig. 3 C and G efficiently, we decompose the velocity field into Littlewood–Paley components and use collocation.

Vorticity-Vector Potential Formulation. We find the vorticity-vector potential formulation of the system 1 of the main text on the three-torus, $\mathbb{T}^3 = S^1 \times S^1 \times S^1$. This is a manifold without boundary, so the usual Hodge decomposition applies (86). For a vector field \mathbf{v} , the decomposition takes the form

$$\mathbf{v} = \nabla \phi + \nabla \wedge \boldsymbol{\psi} + \mathbf{H}, \quad [\text{S3}]$$

where \mathbf{H} is an element of the 3D space of harmonic vector fields, which implies on a torus that $\mathbf{H} = H_x \hat{x} + H_y \hat{y} + H_z \hat{z}$ for some constants H_x, H_y, H_z . For divergence-free flows, we have $\nabla^2 \phi = 0$ and hence $\phi = 0$ because \mathbb{T}^3 is compact and without boundary. In this case, we interpret \mathbf{H} as the fluid center of mass motion. By working in the center of mass frame, we are left with

$$\mathbf{v} = \nabla \wedge \boldsymbol{\psi}. \quad [\text{S4}]$$

Taking the curl of Eq. 1 of the main text gives

$$\partial_t \boldsymbol{\omega} + \mathbf{v} \cdot \nabla \boldsymbol{\omega} - \boldsymbol{\omega} \cdot \nabla \mathbf{v} = \mathcal{L} \boldsymbol{\omega}, \quad [\text{S5}]$$

where $\boldsymbol{\omega} = \nabla \wedge \mathbf{v}$ and

$$\mathcal{L} = \Gamma_0 \nabla^2 - \Gamma_2 \nabla^4 + \Gamma_4 \nabla^6. \quad [\text{S6}]$$

[‡]Structurally similar sixth-order hydrodynamic equations are obtained by systematically reducing magneto-hydrodynamic models in the vicinity of flow bifurcations (Geoffrey Vasil, personal communication).

We can simplify the advection term by using the following standard identity

$$\begin{aligned}\nabla \wedge (\boldsymbol{\omega} \wedge \mathbf{v}) &= \boldsymbol{\omega}(\nabla \cdot \mathbf{v}) - \mathbf{v}(\nabla \cdot \boldsymbol{\omega}) + \mathbf{v} \cdot \nabla \boldsymbol{\omega} - \boldsymbol{\omega} \cdot \nabla \mathbf{v} \\ &= \mathbf{v} \cdot \nabla \boldsymbol{\omega} - \boldsymbol{\omega} \cdot \nabla \mathbf{v},\end{aligned}\quad [\text{S7}]$$

because both fields are divergence-free. This identity speeds up the computational cost of evaluating the advection term, as it requires fewer applications of the fast Fourier transform. Because the divergence of $\boldsymbol{\psi}$ does not affect the decomposition **S3**, we fix the gauge and work with a divergence-free vector potential. In this case, taking the curl of Eq. **S4** gives $\nabla^2 \boldsymbol{\psi} = -\boldsymbol{\omega}$. In summary, in the vorticity-vector potential formulation, the equations of motion read

$$\partial_t \boldsymbol{\omega} + \nabla \wedge (\boldsymbol{\omega} \wedge \mathbf{v}) = \mathcal{L} \boldsymbol{\omega}, \quad [\text{S8a}]$$

$$\nabla^2 \boldsymbol{\psi} = -\boldsymbol{\omega}. \quad [\text{S8b}]$$

Characteristic Scales. The linear growth rate associated with the operator \mathcal{L} is $\sigma(k) = -k^2(\Gamma_0 + \Gamma_2 k^2 + \Gamma_4 k^4)$. For $\Gamma_2 < 0$, the most unstable mode $k_m = \text{argmax} \sigma(k)$ is well approximated by the maximum k_p of the function $f(k) = \sigma(k)/k^2 = -(\Gamma_0 + \Gamma_2 k^2 + \Gamma_4 k^4)$, yielding

$$k_p^2 = \frac{-\Gamma_2}{2\Gamma_4}. \quad [\text{S9}]$$

We prefer to express characteristic scales in terms of k_p (instead of k_m) as this simplifies subsequent formulas, and k_p is generally close to k_m for sufficiently small injection bandwidths. The associated wavelength is $\lambda_p = 2\pi/k_p$. This wavelength represents two vortices, one with positive and one with negative vorticity, each of characteristic diameter

$$\Lambda = \frac{\lambda_p}{2} = \pi \sqrt{\frac{2\Gamma_4}{-\Gamma_2}}. \quad [\text{S10}]$$

The corresponding growth rate is

$$\sigma(k_p) = \frac{\Gamma_2}{2\Gamma_4} \left(\Gamma_0 - \frac{\Gamma_2^2}{4\Gamma_4} \right),$$

which defines the time scale

$$\tau = \frac{1}{\sigma(k_p)}. \quad [\text{S11}]$$

Λ and τ can be used to define a characteristic circulation speed $U = 2\pi\Lambda/\tau$.

Nondimensionalization in Numerical Simulations. For simulation purposes, we rescale time and space as $t = T\tilde{t}$ and $\mathbf{x} = L\tilde{\mathbf{x}}$, where L is the domain size. We further introduce $\boldsymbol{\psi} = \psi_0 \tilde{\boldsymbol{\psi}}$ and $\boldsymbol{\omega} = \omega_0 \tilde{\boldsymbol{\omega}}$. Eqs. **S8** then become (after dropping the tildes)

$$\frac{1}{T} \partial_t \boldsymbol{\omega} + \frac{\psi_0}{L^2} \nabla \wedge (\boldsymbol{\omega} \wedge \mathbf{v}) = \frac{\Gamma_0}{L^2} \left[\nabla^2 \boldsymbol{\omega} - \frac{\Gamma_2}{\Gamma_0 L^2} \nabla^4 \boldsymbol{\omega} + \frac{\Gamma_4}{\Gamma_0 L^4} \nabla^6 \boldsymbol{\omega} \right], \quad [\text{S12a}]$$

$$\frac{\psi_0}{L^2} \nabla^2 \boldsymbol{\psi} = -\omega_0 \boldsymbol{\omega}. \quad [\text{S12b}]$$

Setting $\omega_0 = \frac{1}{T}$, $\psi_0 = \frac{L^2}{T}$, and $T = \frac{L^2}{\Gamma_0}$, and defining $\gamma_2 = \frac{\Gamma_2}{\Gamma_0 L^2}$ and $\gamma_4 = \frac{\Gamma_4}{\Gamma_0 L^4}$, we obtain the nondimensionalized equations

$$\partial_t \boldsymbol{\omega} + \nabla \wedge (\boldsymbol{\omega} \wedge \mathbf{v}) = \nabla^2 \boldsymbol{\omega} - \gamma_2 \nabla^4 \boldsymbol{\omega} + \gamma_4 \nabla^6 \boldsymbol{\omega}, \quad [\text{S13a}]$$

$$\nabla^2 \boldsymbol{\psi} = -\boldsymbol{\omega}. \quad [\text{S13b}]$$

Time Discretization. For the time stepping, we use the third-order semiimplicit backward differentiation scheme introduced by Ascher et al. (87),

$$\begin{aligned}\left(\frac{11}{6} - \Delta t \mathcal{L} \right) \boldsymbol{\omega}^{n+1} &= 3\boldsymbol{\omega}^n - \frac{3}{2}\boldsymbol{\omega}^{n-1} + \frac{1}{3}\boldsymbol{\omega}^{n-2} \\ &\quad - \Delta t (3\mathcal{N}^n - 3\mathcal{N}^{n-1} + \mathcal{N}^{n-2}),\end{aligned}\quad [\text{S14a}]$$

where

$$\mathcal{L} = \nabla^2 - \gamma_2 \nabla^4 + \gamma_4 \nabla^6, \quad [\text{S14b}]$$

$$\mathcal{N}(\boldsymbol{\psi}, \boldsymbol{\omega}) = \nabla \wedge (\boldsymbol{\omega} \wedge \mathbf{v}), \quad [\text{S14c}]$$

recalling that $\mathbf{v} = \nabla \wedge \boldsymbol{\psi}$. We then solve for the vector potential

$$\nabla^2 \boldsymbol{\psi}^{n+1} = -\boldsymbol{\omega}^{n+1}. \quad [\text{S15}]$$

Space Discretization. We work with a Fourier spectral method. If we denote the rhs of Eq. **S14a** by \mathbf{b}^{n+1} , then the update formula for the Fourier coefficients reads

$$\boldsymbol{\omega}^{n+1}(\mathbf{k}) = \frac{1}{p(\mathbf{k})} \mathbf{b}^{n+1}(\mathbf{k}), \quad [\text{S16a}]$$

$$\boldsymbol{\psi}^{n+1}(\mathbf{k}) = \frac{1}{k^2} \boldsymbol{\omega}^{n+1}(\mathbf{k}), \quad [\text{S16b}]$$

where $p(\mathbf{k}) = 11/6 + \Delta t(k^2 + \gamma_2 k^4 + \gamma_4 k^6)$. In addition, we always have $\boldsymbol{\omega}(t, \mathbf{k} = 0) = 0$, because the vorticity is defined by taking the curl of \mathbf{v} , and we can set $\boldsymbol{\psi}(t, \mathbf{k} = 0) = 0$ by gauge freedom. Because both $\boldsymbol{\omega}$ and $\boldsymbol{\psi}$ are divergence-free, we have to impose

$$\mathbf{k} \cdot \boldsymbol{\omega} = 0, \quad \mathbf{k} \cdot \boldsymbol{\psi} = 0. \quad [\text{S17}]$$

If we initiate the simulations with divergence-free fields, then the update rule **S16** preserves this property in exact arithmetic. Nevertheless, numerical errors will always build up after several iterations in double-precision arithmetic. We project back onto the divergence-free manifold every several steps by mimicking gauge transformation. Suppose $\boldsymbol{\omega}$ has small divergence that we want to remove. We set $f = \nabla \cdot \boldsymbol{\omega}$. We then solve the Poisson equation,

$$\nabla^2 \lambda = f, \quad [\text{S18}]$$

and subsequently remove the divergence from $\boldsymbol{\omega}$ according to

$$\boldsymbol{\omega} \rightarrow \boldsymbol{\omega} - \nabla \lambda. \quad [\text{S19}]$$

Calculation of Shell Interactions. We next explain how the energy spectra, fluxes, and energy flow tables are calculated numerically (Fig. 3 of the main text and Fig. S3). To establish notation, we first recall the derivation of the energy balance equation as given in Waleffe (19). Expanding the velocity and pressure fields in Fourier series, Eq. **1** of the main text give

$$k_i \cdot v_i(t, \mathbf{k}) = 0,$$

$$[\partial_t + \xi(\mathbf{k})] v_i(t, \mathbf{k}) = -ik_i p(t, \mathbf{k}) - i \sum_{\mathbf{q}+\mathbf{p}=\mathbf{k}} v_j(t, \mathbf{p}) q_j v_i(t, \mathbf{q}),$$

where $\xi(\mathbf{k}) = \Gamma_0 k^2 + \Gamma_2 k^4 + \Gamma_4 k^6$. By projecting on helical modes one finds Eq. **3** of the main text. To find the equation for the energy in mode \mathbf{k} we relabel $\mathbf{k} \rightarrow -\mathbf{k}$ in the second equation, multiply by $v_i(t, \mathbf{k})$, sum over i , and use the incompressibility condition to get

$$v_i(\mathbf{k}) [\partial_t + \xi(\mathbf{k})] v_i(-\mathbf{k}) = -i \sum_{\mathbf{k}+\mathbf{p}+\mathbf{q}=0} v_j(\mathbf{p}) q_j v_i(\mathbf{q}) v_i(\mathbf{k}),$$

where we dropped the explicit time dependence for ease of notation. We now add the above equation to its complex conjugate and use $v_i(-\mathbf{k}) = \bar{v}_i(\mathbf{k})$,

$$[\partial_t + 2\xi(\mathbf{k})] |v(\mathbf{k})|^2 = -i \sum_{\mathbf{k}+\mathbf{p}+\mathbf{q}=0} v_j(\mathbf{p}) q_j v_i(\mathbf{q}) v_i(\mathbf{k}) + \text{c.c.}$$

The energy in shell $|\mathbf{k}| = k$ is defined as

$$\epsilon(t, k) = \frac{1}{2} \sum_{|\mathbf{k}'|=k} |v(t, \mathbf{k}')|^2. \quad [\text{S20}]$$

The corresponding evolution equation is

$$[\partial_t + 2\xi(k)]\epsilon(t, k) = \sum_p \sum_q \tilde{t}(t; k, p, q),$$

where

$$\begin{aligned} \tilde{t}(t; k, p, q) &= -\frac{i}{2} \sum_{\substack{\text{shells} \\ k, p, q}} \delta_{k+p+q, 0} v_j(t, \mathbf{p}) q_j v_i(t, \mathbf{q}) v_i(t, \mathbf{k}) + \text{c.c.} \\ &= -i \sum_{\substack{\text{shells} \\ k, p, q}} \delta_{k+p+q, 0} v_j(t, \mathbf{p}) q_j v_i(t, \mathbf{q}) v_i(t, \mathbf{k}). \end{aligned} \quad [\text{S21}]$$

We used the fact that the sum over all modes can be split into radial and shell parts $\sum_{\mathbf{k}} f(\mathbf{k}) = \sum_k \sum_{|\mathbf{k}'|=k} f(\mathbf{k}')$ and we defined

$$\sum_{\substack{\text{shells} \\ k, p, q}} f(\mathbf{k}, \mathbf{q}, \mathbf{p}) \equiv \sum_{|\mathbf{k}'|=k} \sum_{|\mathbf{p}'|=p} \sum_{|\mathbf{q}'|=q} f(\mathbf{k}', \mathbf{q}', \mathbf{p}').$$

Symmetrizing as $t(t; k, p, q) = \tilde{t}(t; k, p, q) + \tilde{t}(t; k, q, p)$ gives the usual energy balance equation (1, 19)

$$[\partial_t + 2\xi(k)]\epsilon(t, k) = T(t, k), \quad [\text{S22a}]$$

where

$$T(t, k) = \frac{1}{2} \sum_p \sum_q t(t; k, p, q). \quad [\text{S22b}]$$

The quantity $t(t; p, k, q)$ is the energy transfer into the shell k due to all triad interactions with shells p and q at time t , and $T(t, k)$ is the energy transfer into the shell k due to all triad interactions. The energy flux across k is defined as

$$\Pi(t, k) = \sum_{k' > k} T(t, k') \quad [\text{S23}]$$

and represents energy flow from wavenumbers below k to those above it at time t .

Projecting the velocity field onto the helical modes reveals additional substructure (19). The energy spectrum splits into two helical components

$$\epsilon(t, k) = \epsilon^+(t, k) + \epsilon^-(t, k), \quad \epsilon^\pm(t, k) = \sum_{|\mathbf{k}'|=k} |u^\pm(t, \mathbf{k}')|^2. \quad [\text{S24}]$$

The energy flow and energy flux split into eight components, one for each possible assignment of the helicity index over the triads

$$\begin{aligned} t(t; k, p, q) &= \sum_{i=1}^8 t^{(i)}(t; k, p, q), \quad T(t; k) = \sum_{i=1}^8 T^{(i)}(t; k), \\ \Pi(t, k) &= \sum_{i=1}^8 \Pi^{(i)}(t, k), \end{aligned} \quad [\text{S25}]$$

where we follow the binary ordering as in ref. 19 ($i = 1$ corresponds to $+++$, $i = 2$ to $++-$, etc.). The energy conservation for helical shells becomes

$$[\partial_t + 2\xi(k)]\epsilon^\pm(t, k) = T^\pm(t, k), \quad [\text{S26}]$$

where $T^+(t, k) = \sum_{i=1}^4 T^{(i)}(t, k)$ and $T^-(t, k) = \sum_{i=5}^8 T^{(i)}(t, k)$.

We now consider time averages. For a quantity \mathcal{O} we define

$$\langle \mathcal{O} \rangle = \lim_{\mathcal{R}, \Delta \rightarrow \infty} \frac{1}{\Delta} \int_{\mathcal{R}}^{\mathcal{R}+\Delta} dt \mathcal{O}(t). \quad [\text{S27}]$$

In practice, \mathcal{R} is the relaxation time for the system, and Δ is the length of the averaging interval. In the stationary regime, the averages become time independent, which we denote by

$$\langle \epsilon(t, k) \rangle = \langle \epsilon(k) \rangle, \quad \langle t(t; k, p, q) \rangle = \langle t(k, p, q) \rangle \quad [\text{S28}]$$

and

$$\langle \partial_t \epsilon(t, k) \rangle = \partial_t \langle \epsilon(t, k) \rangle = 0. \quad [\text{S29}]$$

Taking averages reduces Eq. S22a to

$$2\xi(k) \langle \epsilon(k) \rangle = \langle T(k) \rangle. \quad [\text{S30}]$$

Thus, in the stationary regime, the energy flux can be derived from the spectrum according to

$$\langle \Pi(k) \rangle = \sum_{k' > k} 2\xi(k') \langle \epsilon(k') \rangle. \quad [\text{S31}]$$

Similarly, for the helical projections we get

$$2\xi(k) \langle \epsilon^\pm(k) \rangle = \langle T^\pm(k) \rangle, \quad [\text{S32}]$$

and

$$\langle \Pi^\pm(k) \rangle = \sum_{k' > k} 2\xi(k') \langle \epsilon^\pm(k') \rangle. \quad [\text{S33}]$$

We numerically estimate the discrete stationary spectra $\langle \epsilon^\pm(k) \rangle$ as follows. At each time step n , we calculate

$$\epsilon_n^\pm(k) = \sum_{|\mathbf{k}'|=k} |u_n^\pm(\mathbf{k}')|^2. \quad [\text{S34}]$$

We then apply the discrete version of the formula S27,

$$\langle \epsilon^\pm(k) \rangle_{\mathcal{R}, \Delta} = \frac{1}{\Delta} \sum_{n=\mathcal{R}}^{\mathcal{R}+\Delta} \epsilon_n^\pm(k), \quad [\text{S35}]$$

where we choose \mathcal{R} to be the relaxation time of the energy and helicity time series and the averaging interval Δ is taken long enough to ensure convergence of statistical observables (Fig. S2). We recover the helical flux contributions using formula S32 and the total flux from $\langle \Pi(k) \rangle = \langle \Pi^+(k) \rangle + \langle \Pi^-(k) \rangle$.

For plotting purposes, we connect the discrete energy spectra to their continuous definitions. The mean kinetic energy in the system of size L is

$$E = \sum_k \epsilon(k) = \sum_{\tilde{k}} \frac{\sum_{k' \in [\tilde{k}, \tilde{k}+\Delta k)} \epsilon(k')}{\Delta k} \Delta k, \quad [\text{S36}]$$

where $\tilde{k} = n \frac{2\pi}{L}$, $n = 1, 2, 3, \dots$ and $\Delta k = \frac{2\pi}{L}$. In the limit $L \rightarrow \infty$, we recover the continuous definition of the energy spectrum

$$E = \int_0^\infty e(\tilde{k}) d\tilde{k}, \quad [\text{S37}]$$

$$e(\tilde{k}) = \lim_{L \rightarrow \infty} \sum_{k' \in [\tilde{k}, \tilde{k}+\Delta k)} \frac{\epsilon(k')}{\Delta k}. \quad [\text{S38}]$$

When plotting energy spectra, we thus use the discrete (finite box size) approximation of the continuous definition

$$\epsilon^\pm(\tilde{k}) = \frac{\sum_{k' \in [\tilde{k}, \tilde{k}+\Delta k)} \langle \epsilon^\pm(k') \rangle_{\mathcal{R}, \Delta}}{\Delta k}. \quad [\text{S39}]$$

The spectral domains I, II, and III in Fig. 1A of the main text have finite thickness. To calculate the energy flow between the regions, we have to sum over shells contained in a given region. For example,

$$\mathcal{T}_{\text{I,II,III}} = \frac{1}{2} \sum_{k \in \text{region I}} \sum_{p \in \text{region II}} \sum_{q \in \text{region III}} t(k, p, q) \quad [\text{S40}]$$

is the energy flow into region I due to all triad interactions with modes supported on regions II and III. To calculate $\mathcal{T}_{K PQ}$, where $K, P, Q \in \{\text{I, II, III}\}$, consider the following integral,

$$\tilde{\mathcal{T}}_{K PQ} = - \int d^3x \mathbf{v}_K \cdot [(\mathbf{v}_P \cdot \nabla) \mathbf{v}_Q], \quad [\text{S41}]$$

where \mathbf{v}_K is the Littlewood–Paley component corresponding to region K and similarly for \mathbf{v}_P and \mathbf{v}_Q . Specifically, \mathbf{v}_K is obtained from \mathbf{v} by keeping only the Fourier amplitudes supported on the region K , etc. In terms of Fourier series, we find that

$$\tilde{\mathcal{T}}_{K PQ} = \sum_{k \in \text{region } K} \sum_{p \in \text{region } P} \sum_{q \in \text{region } Q} \tilde{t}(k, p, q), \quad [\text{S42}]$$

where $\tilde{t}(k, p, q)$ is given by Eq. S21. We symmetrize in the last to indexes, by defining

$$\mathcal{T}_{K PQ} = \frac{1}{2} (\tilde{\mathcal{T}}_{K PQ} + \tilde{\mathcal{T}}_{K QP}). \quad [\text{S43}]$$

To split $\mathcal{T}_{K PQ} = \sum_{i=1}^8 \mathcal{T}_{K PQ}^{(i)}$ into the contributions from the eight types of helical triad interactions, it is convenient to consider equivalent integral representations of the form

$$\tilde{\mathcal{T}}_{K PQ}^{s_K s_P s_Q} = - \int d^3x \mathbf{v}_K^{s_K} \cdot [(\mathbf{v}_P^{s_P} \cdot \nabla) \mathbf{v}_Q^{s_Q}], \quad [\text{S44}]$$

where $\mathbf{v}_K^{s_K}$ is constructed from \mathbf{v}_K by projection onto modes with helicity index $s_K \in \{\pm\}$, etc. The symmetrization

$$\mathcal{T}_{K PQ}^{s_K s_P s_Q} = \frac{1}{2} (\tilde{\mathcal{T}}_{K PQ}^{s_K s_P s_Q} + \tilde{\mathcal{T}}_{K QP}^{s_K s_Q s_P}), \quad [\text{S45}]$$

represents the energy flow into modes with helicity index s_K lying in region K , due to interactions with modes with helicity indexes s_P and s_Q in regions P and Q , respectively. Expressions of the form S44 are calculated, at a given time step, by collocation: Evaluate the three projections in the physical domain on an equally spaced grid, perform the point-wise multiplication, go back to Fourier space, and integrate by reading off the value of the zeroth Fourier mode. All these operations are done efficiently using the fast Fourier transform. To calculate the stationary energy flows $\langle \mathcal{T}_{K PQ}^{s_K s_P s_Q} \rangle$ shown in the energy flow tables (Fig. 3 C and G in the main text and Fig. S3C), we adopt a procedure analogous to that used to estimate the energy spectra.

Cascade Characteristics

The phenomenology of the inverse cascade in passive 2D turbulent flows is often characterized in terms of vortex mergers. By contrast, in active fluids with a well-defined vortex scale Λ and a small injection bandwidth κ_S , vortex mergers are suppressed by the dominant pattern-scale selection processes. This raises the question how the inverse cascade, which can transport a considerable fraction of energy to larger scales (Fig. S4E), manifests itself in the flow-field structure of a 3D active fluid. Our simulations demonstrate that pattern-forming nonequilibrium fluids can achieve energy transport to larger scales by forming chain-like vortex complexes that propagate through the fluid (Movie S1). To illustrate this phenomenon in more detail, Fig. S4 A–D shows two horizontal 2D (x, y) slices of a large 3D simulation domain (size $L = 32\Lambda$) at a fixed representative time for an active fluid with small active bandwidth κ_S (using the same parameters as in the main text). In Fig. S4 A and B, the flow field is visualized through the perpendicular z component of the vorticity, ω_z , and in Fig. S4 C and D through the local helicity h . The thin black lines in Fig. S4 A and B indicate in-plane portions of filaments consisting of alternating vortices that correspond to 3D filamentous clusters of high helicity in Fig. S4 C and D. The kinetic energy transported to large scales manifests itself as the formation and motion of such vortex chains (Movie S1). These results illustrate that the helicity-driven 3D inverse cascade in active fluids is distinctly different from the energy-driven 2D inverse cascade in passive fluids.

A detailed spectral characterization of this helicity-driven 3D active turbulence can be obtained by analyzing the upward energy transfer into region I in Fourier space (defined in Fig. 1A of the main text). Fig. S4E shows the absolute value of the energy flux for an active fluid with small bandwidth κ_S for three different simulation domain sizes. In the case of an inertial energy cascade, one expects the flux to be independent of the wavenumber k , at least over some range. In such inertial ranges there is no dissipation of energy, just purely nonlinear redistribution. In our simulations, we see that the energy flux, upon entering the spectral region I from above (i.e., coming from region II), is at first noninertial with an approximate k^3 scaling, implying that the transfer is assisted by strong dissipation effects. At very large scales $\gg \Lambda$, however, the flux develops a plateau, indicating that the transfer becomes mostly inertial. Increasing the simulation domain size broadens the plateau and increases the magnitude of the flux that reaches the plateau. Interestingly, at these very large scales, the model defined in Eq. 1 of the main text effectively reduces to the classical Navier–Stokes equations.

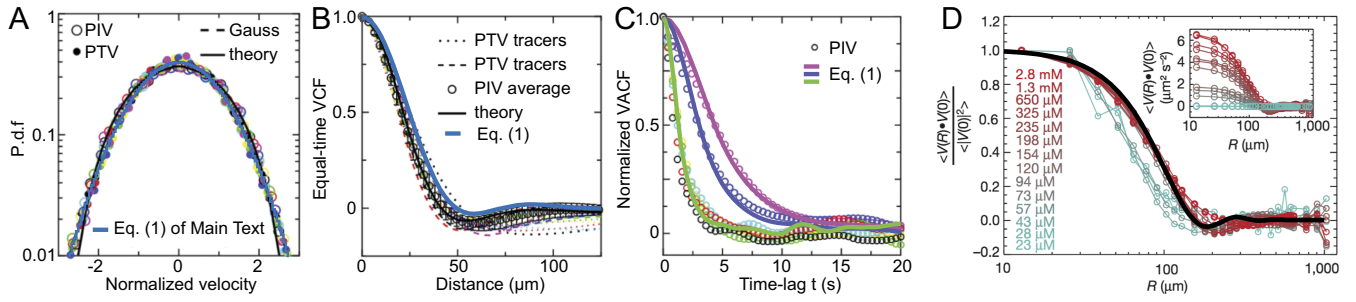


Fig. S1. Fit results for the generalized Navier–Stokes model defined in Eq. 1 of the main text compared with recent experimental data for (A–C) bacterial suspensions and (D) microtubule networks. (A) PDFs of the Cartesian in-plane velocity components, normalized by their mean values and standard deviations. The black curve labeled “theory” represents a five-parameter continuum model for the bacterial dynamics described in ref. 35. The blue curve is obtained for the generalized three-parameter Navier–Stokes model of the solvent flow defined in Eq. 1 of the main text, using the fit parameters listed in the description of C. Note that only the Navier–Stokes model correctly captures the tails of the velocity distribution. (B) The equal-time VCFs indicate the characteristic pattern formation scale. The black curve labeled “theory” again represents the continuum model for the bacterial dynamics described in ref. 35. The blue curve is obtained for the Navier–Stokes model for the solvent flow defined in Eq. 1 of the main text, using the fit parameters listed in the description of C. (C) VACFs obtained for three different values of the fit parameters corresponding to three different activity levels of the bacteria: $\Gamma_0 = 4.77 \mu\text{m}^2/\text{s}$, $\Gamma_2/\Gamma_0 = -1.15 \times 10^3 \mu\text{m}^2$, $\Gamma_4/\Gamma_0 = 9.80 \times 10^4 \mu\text{m}^4$ (magenta line), $\Gamma_0 = 6.82 \mu\text{m}^2/\text{s}$, $\Gamma_2/\Gamma_0 = -1.15 \times 10^3 \mu\text{m}^2$, $\Gamma_4/\Gamma_0 = 9.80 \times 10^4 \mu\text{m}^4$ (blue lines), $\Gamma_0 = 1.59 \times 10^1 \mu\text{m}^2/\text{s}$, $\Gamma_2/\Gamma_0 = -1.15 \times 10^3 \mu\text{m}^2$, and $\Gamma_4/\Gamma_0 = 9.80 \times 10^4 \mu\text{m}^4$ (green line). In terms of the characteristic vortex size Λ , growth time τ , speed U , and bandwidth κ , these parameters correspond to $\Lambda = 41 \mu\text{m}$, $\tau = 15 \text{ s}$, $U = 17.2 \mu\text{m}/\text{s}$, and $\kappa = 73 \text{ mm}^{-1}$ (magenta); $\Lambda = 41 \mu\text{m}$, $\tau = 10.5 \text{ s}$, $U = 24.5 \mu\text{m}/\text{s}$, and $\kappa = 73 \text{ mm}^{-1}$ (blue); and $\Lambda = 41 \mu\text{m}$, $\tau = 4.5 \text{ s}$, $U = 57.2 \mu\text{m}/\text{s}$, and $\kappa = 73 \text{ mm}^{-1}$ (green). (D) Equal-time VCF for an active fluid driven by a microtubule network. The black line is obtained for the Navier–Stokes model for the solvent flow defined in Eq. 1 of the main text, using fit parameters $\Gamma_0 = 9.05 \times \mu\text{m}^2/\text{s}$, $\Gamma_2/\Gamma_0 = -8.61 \times 10^3 \mu\text{m}^2$, $\Gamma_4/\Gamma_0 = 7.37 \times 10^6 \mu\text{m}^4$ corresponding to $\Lambda = 130 \mu\text{m}$, $\tau = 125 \text{ s}$, $U = 6.5 \mu\text{m}/\text{s}$, and $\kappa = 21 \text{ mm}^{-1}$. All simulations were performed on a large 3D domain of size $L = 32\Lambda$ to exclude finite size effects. A–C were reprinted with permission from ref. 35. D was reprinted from ref. 38 by permission from Macmillan Publishers Ltd: *Nature*, copyright (2012).

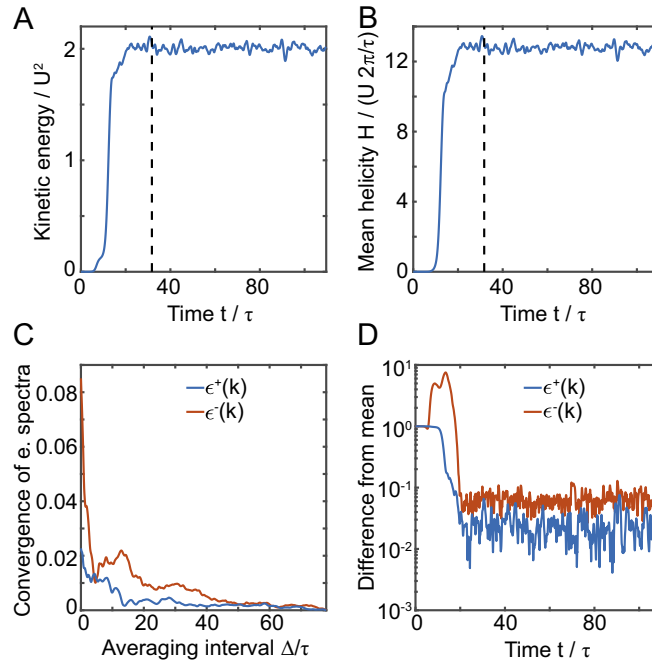


Fig. S2. Numerical estimation of the stationary energy spectra for the narrow bandwidth in Fig. 3A of the main text. (A and B) Kinetic energy (A) and helicity time series (B) are used to determine the relaxation time \mathcal{R} to stationary state (vertical dashed line, $\mathcal{R} = 31.7$ in this case). (C) Convergence of the energy spectra estimates using $|\langle \epsilon^\pm \rangle_{\mathcal{R}, \Delta} - \langle \epsilon^\pm \rangle_{\mathcal{R}, \Delta_{\max}}| / |\langle \epsilon^\pm \rangle_{\mathcal{R}, \Delta_{\max}}|$ (Eq. S35), as a function of the averaging interval Δ . (D) Relative difference (l^2 norm) between the momentary energy spectra and their (stationary) mean as a function of time.

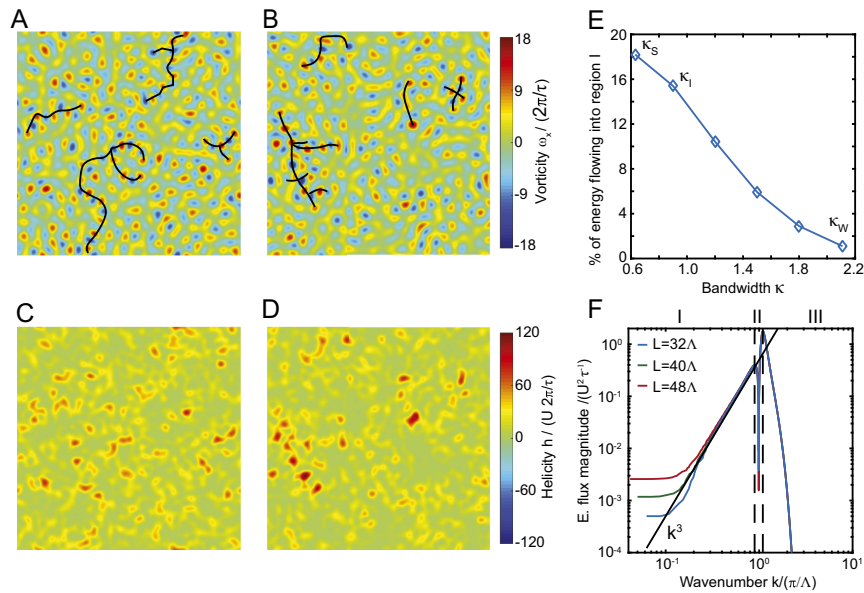


Fig. 54. Characterization of the inverse energy cascade. (A and B) Two horizontal cuts through the 3D simulation domain for a small bandwidth κ_S , showing that the inverse cascade is not characterized by vortex mergers, but rather by chain-like complexes, visible as “dark” structures in Movie S1, Left. (C and D) Same flow-field snapshots as in A and B but now represented through the local helicity field. The chain-like large-scale structures carry most of the helicity. They do not merge, but rather form extended filaments and clusters that move throughout the simulation domain (Movie S1). Domain size $L = 32\Lambda$. (E) The proportion of the energy injected by the active component that is transported to region I (corresponding to large scales, compare with Fig. 1A of the main text) as a function of the active bandwidth κ . (F) Absolute value of the energy flux for an active fluid with small bandwidth κ_S for different simulation domain sizes. In region I, corresponding to large scales, the upward transfer is noninertial at intermediate wavenumbers with the flux exhibiting k^3 scaling. For $k \rightarrow 0$, however, the flux approaches a constant plateau value, indicating that inertial effects start dominate at very large scales $\gg \Lambda$.

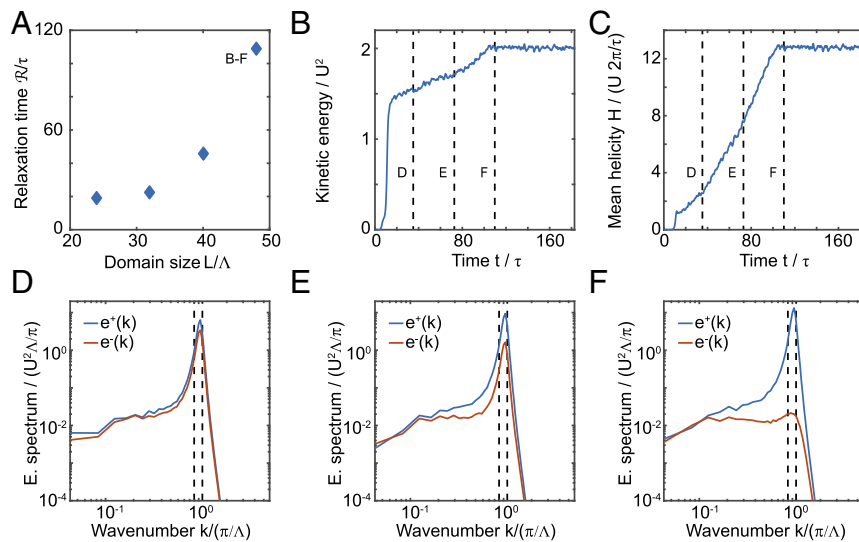
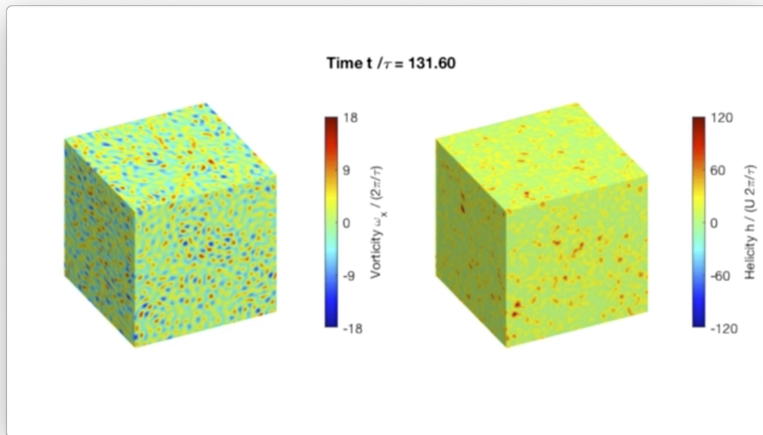


Fig. 55. (A) Relaxation time for spontaneous symmetry breaking depends on the domain size. (B and C) Kinetic energy (B) and helicity (C) as a function of time for a very large domain ($L = 48\Lambda$). The relaxation proceeds in two stages, the initial stage characterized by a rapid exponential growth rate ($t < 20\tau$), followed by a slower linear growth until full relaxation ($t \approx 100\tau$). (D–F) Energy spectra at various stages of the relaxation process (compare with dashed lines in B and C) show how the system realizes a state with broken mirror symmetry.



Movie S1. The turbulent steady-state flow dynamics for an active fluid with small energy injection bandwidth $\kappa = 0.63/\Lambda$ as typically observed in our 3D simulations. This simulation was performed in a cubic box of size $L = 32\Lambda$, where Λ is the typical vortex scale, using unbiased random initial conditions and periodic boundary conditions. *Left* shows a component of the vorticity pseudovector and *Right* shows the corresponding local helicity field. Note that the measured values of the helicity are predominantly positive everywhere, indicating that the flow has undergone spontaneous mirror-symmetry breaking to realize a near-Beltrami vector field. Extended chain-like clusters of high vorticity and helicity transport the energy from smaller to larger scales.

[Movie S1](#)